

Showcasing research in Analytical Micro and Nano Technologies from Professor Alberto Escarpa's laboratory, Department of Analytical Chemistry, Physical Chemistry and Chemical Engineering, University of Alcalá, Madrid, Spain.

A dual colorimetric-electrochemical microfluidic paper-based analytical device for point-of-care testing of ischemic strokes

We propose a microfluidic paper-based analytical device for the reliable assessment of transferrin saturation biomarker (TSAT) integrating both Fe colorimetric (left side brain) and Tf electrochemical (right side brain) detection. The integrated dual colorimetric-electrochemical paper chip becomes promising point-of-care testing to assist physicians in the fast diagnosis and prognosis of ischemic stroke, where the time to decide is crucial for a patient's survival. Image credit: Silvia Dorte, Marta Pacheco and Alberto Escarpa. Copyright holders: Silvia Dorte, Marta Pacheco, Teresa Gasull, Agustín G. Crevillen, Alberto Escarpa

### As featured in:








See Alberto Escarpa *et al.*,  
*Lab Chip*, 2024, **24**, 4253.



Cite this: *Lab Chip*, 2024, 24, 4253

# A dual colorimetric-electrochemical microfluidic paper-based analytical device for point-of-care testing of ischemic strokes†

Silvia Dorte, <sup>a</sup> Marta Pacheco, <sup>b</sup> Teresa Gasull, <sup>c</sup>  
 Agustín G. Crevillen <sup>\*d</sup> and Alberto Escarpa <sup>\*ae</sup>

A novel microfluidic paper-based analytical device with dual colorimetric and electrochemical detection (dual  $\mu$ PAD) was developed for the assessment of transferrin saturation (TSAT) in samples from ischemic stroke patients. TSAT was calculated from the ratio between transferrin-bound iron, which was colorimetrically measured, and the total iron-binding capacity, which was electrochemically measured. To this end, a  $\mu$ PAD was smartly designed, which integrated both colorimetric and electrochemical detection reservoirs, communicating via a microchannel acting as a chemical reactor, and with preloading/storing capabilities (reagent-free device). This approach allowed the dual and simultaneous determination of both parameters, providing an improvement in the reliability of the results due to an independent signal principle and processing. The  $\mu$ PADs were validated by analyzing a certified reference material, showing excellent accuracy ( $E_r \leq 5\%$ ) and precision ( $RSD \leq 2\%$ ). Then they were applied to the analysis of diagnosed serum samples from ischemic stroke patients. The results were compared to those provided by a free-interference method (urea-PAGE). Impressively, both methods exhibited a good correlation ( $r = 0.96$ ,  $p < 0.05$ ) and no significant differences were found between them (slope  $1.0 \pm 0.1$  and the intercept  $1 \pm 4$ ,  $p < 0.05$ ), demonstrating the excellent accuracy of our approach during the analysis of complex samples from ischemic stroke patients, using just 90  $\mu$ L of clinical samples and taking less than 90 min in comparison with the 18 hours required by the urea-PAGE approach. The developed fully integrated colorimetric-electrochemical  $\mu$ PAD is a promising ready to use reagent-free device for the *point-of-care* testing of TSAT, which can be used to assist physicians in the fast diagnosis and prognosis of ischemic strokes, where the decision-time is crucial for the patient's survival.

Received 6th May 2024,  
 Accepted 29th July 2024

DOI: 10.1039/d4lc00398e

rsc.li/loc

## Introduction

Ischemic stroke is one of the leading causes of death and serious disability. According to the World Health Organization (WHO), annually, 15 million people worldwide suffer a stroke.<sup>1</sup>

Ischemic strokes are caused by vascular occlusion in the brain producing an inadequate blood supply to the brain tissues, causing loss of their functionality and ultimately a cerebral infarction. This ischemia generates neuronal death with the loss of electrical function and progresses through the generation of reactive oxygen species (ROS), destruction of cell membranes, and cell lysis. The progression of cerebral tissue towards an infarction depends on the magnitude and duration of the drop in cerebral blood flow and generally causes neuronal dysfunction leading to ischemic symptoms, typically motor function deficits such as loss of strength, sensitivity or tingling in parts of the body, difficulty speaking or altered mental status in patients.<sup>2</sup>

The clinical diagnosis of patients who have suffered an ischemic stroke is a medical emergency that requires immediate treatment within a limited period. It is usually diagnosed rapidly by non-contrast computed tomography (CT) due to its wide availability and relatively short imaging time,<sup>3</sup> magnetic resonance imaging (MRI) although it has generally limited availability, or by careful clinical assessment (clinical history and neurological examination).<sup>4</sup> The problem is that the

<sup>a</sup> Department of Analytical Chemistry, Physical Chemistry and Chemical Engineering, University of Alcalá, 28802, Alcalá de Henares, Madrid, Spain.  
 E-mail: alberto.escarpa@uah.es

<sup>b</sup> Department of Chemistry in Pharmaceutical Sciences, Analytical Chemistry, Faculty of Pharmacy, Complutense University of Madrid, 28040 Madrid, Spain

<sup>c</sup> Cellular and Molecular Neurobiology Research Group, Department of Neurosciences, Germans Trias i Pujol Research Institute (IGTP), 08916, Badalona, Barcelona, Spain

<sup>d</sup> Department of Analytical Sciences, Faculty of Sciences, Universidad Nacional de Educación a Distancia (UNED), 28040, Madrid, Spain.

E-mail: agustingcrevillen@ccia.uned.es

<sup>e</sup> Chemical Research Institute "Andrés M. Del Río" (IQAR), University of Alcalá, 28802, Alcalá de Henares, Madrid, Spain

† Electronic supplementary information (ESI) available. See DOI: <https://doi.org/10.1039/d4lc00398e>

‡ Both authors contributed equally.



frequency of stroke mimics admissions in emergencies is usually very high. Moreover, tests such as simple CT are usually not informative, MRI gives many false negatives, and neurological examinations are sometimes impossible due to the consequences of brain damage induced by ischemia.<sup>5–7</sup> For all these reasons, a differential diagnosis of ischemia *versus* other etiologies is required. In this context, biomarkers are valuable tools to support the clinical diagnosis of stroke, not only to guide treatment and prognosis, but also to identify patients at risk of the disease.

Most of the biomarkers used for the diagnosis and prognosis of ischemic stroke are proteins related to the pathophysiology of the disease, such as damage to brain tissue, inflammation, endothelium, and coagulation/thrombosis.<sup>8–11</sup> The role of tissue iron stores appears crucial, as clinical studies have found evidence of ferroptosis-related brain damage in patients with acute ischemic stroke.<sup>12–14</sup> Moreover, it was demonstrated that higher iron status was associated with an increased risk of stroke<sup>15</sup> and with a detrimental effect on functional outcomes after ischemic stroke.<sup>16</sup>

Iron is an essential element for the growth and survival of almost all living organisms. It is involved in many biological processes due to its inherent redox properties between ferrous, *i.e.* Fe<sup>2+</sup>, and ferric, *i.e.* Fe<sup>3+</sup>, states.<sup>17</sup> The iron form concentration must be tightly regulated by all organisms within the body to avoid the drastic consequences of iron deficiency or excess.<sup>18–20</sup> In blood, most of the iron is bound to transferrin (Tf) (one Tf molecule can bind two Fe<sup>3+</sup> ions), which transports iron in a soluble and non-toxic form throughout the body.<sup>21,22</sup> Tf plays a vital role in iron metabolism in the body. Its main function is the transport of iron from sites of absorption, utilization, or storage to various tissues. In addition, it maintains Fe<sup>3+</sup> in a soluble form under physiological conditions, which protects against the toxic side effects of ROS.<sup>21,23–26</sup> Tf concentration in human serum is approximately 2–3 g L<sup>−1</sup>. Tf levels may also be related to body iron stores, since in the case of iron deficiency (anemia) an increase in the Tf level is observed. By contrast, a decrease in the Tf level is observed with iron overload.<sup>25–27</sup>

In this sense, transferrin saturation (TSAT) is considered an important biomarker of general body iron status since it can be used to diagnose iron deficiency and iron overload in combination with other serum biomarkers such as ferritin.<sup>22,28</sup> Moreover, a high level of TSAT is related to an increased risk of stroke<sup>15</sup> and brain damage induced by ischemia.<sup>29–34</sup> In the latter scenario, a high level of TSAT (more than 30%) in patients during the critical first hours post-ischemic stroke onset means a worse ischemic stroke prognosis, as has been demonstrated in basic and clinical research.<sup>29</sup>

TSAT (%) is defined as the ratio between the amount of serum iron and the total iron-binding capacity (TIBC, the maximum amount of iron that can be captured by Tf):<sup>22</sup>

$$\text{TSAT (\%)} = \frac{\text{serum iron}}{\text{TIBC}} \times 100 \quad (1)$$

Among the various methods for measurement of serum iron, direct colorimetric methods using ferrozine or

bathophenanthroline chromophores are widely used for routine analysis.<sup>22,35,36</sup> However, TIBC can be measured using direct or indirect methods. Regarding the direct methods, the assay consists of the addition of an excess amount of ferric iron to the serum sample to saturate all the free sites on Tf, followed by the removal of excess ferric iron unbound to Tf and finally the iron that fully saturates the Tf is measured colorimetrically.<sup>22,35,37</sup> Regarding indirect methods, TIBC can be measured using unsaturated iron-binding capacity (UIBC) or by using Tf concentration. In the first one, TIBC is calculated as the sum of serum iron concentration and UIBC (which is the additional amount of Fe<sup>3+</sup> necessary to fully saturate all free active sites of Tf) and both parameters are measured colorimetrically (TIBC = serum iron + UIBC).<sup>22,36</sup> Indirect methods to calculate TIBC using Tf concentration usually involve immunochemical or electrochemical measurement of Tf. Each mol of Tf (with an average molecular weight of 79.5 kDa) can bind 2 mol of iron (with a molecular weight of 55.8 Da). That is, a Tf concentration of 1 g L<sup>−1</sup> is equivalent to 12.57 μmol L<sup>−1</sup> of Tf, so it should be able to bind 25.1 μmol L<sup>−1</sup> of iron.<sup>22,37</sup> Therefore, TIBC can be calculated by multiplying the Tf concentration (in g L<sup>−1</sup>) by a conversion factor (25.1 for TIBC in μmol L<sup>−1</sup> or 1.4 for TIBC in μg mL<sup>−1</sup>):<sup>22</sup>

$$\text{TIBC} = [\text{Tf}] \times \text{conversion factor} \quad (2)$$

However, there are great differences in the TSAT values of up to 35% among commercial methods since they assume that all serum iron is bound to Tf and this is not right.<sup>38,39</sup> The urea polyacrylamide gel electrophoresis (urea-PAGE) overcomes this handicap, because it separates and directly detects the different Tf forms (apo-Tf, monoferric-Tf, and diferric-Tf), showing higher accuracy and reliability than the aforementioned methods.<sup>30,40,41</sup> Unfortunately, this technique requires skilled personnel, and it is slow and laborious (low automation), so it is performed in clinical or centralized laboratories.

Therefore, the development of fast and reliable methods for determining TSAT is much needed, with special emphasis on simplicity, low-cost, and portability. These features would allow clinicians to use them for *point-of-care* testing (POCT), providing fast information and assisting in urgent decision-making such as the diagnosis/prognosis of ischemic stroke. In this context, paper-based analytical devices (PADs) offer several advantages such as portability, operational simplicity, miniaturization, biocompatibility, low-cost, ease of use, and availability, which make them perfect platforms for POCT.<sup>42,43</sup> In addition, microfluidic paper-based analytical devices (μPADs) have other advantages inherent to microfluidic technology such as spatial control of fluids by using microchannels and chambers, and multiplexing by creating multiple detection reservoirs.<sup>44,45</sup> Among detection modes employed in PADs, colorimetric and electrochemical detection methods are the most widely used. The colorimetric approach offers sensitivity, adaptability, and cost effectiveness, and it can be implemented on a smartphone, so it is attracting enormous attention from the scientific





community for its simple quantitative analysis, portability, and connectivity.<sup>46,47</sup> The electrochemical approach, commonly known as electrochemical paper-based analytical devices (ePADs), satisfies many of the requirements for *in situ* measurements due to portability and low power demands. These electrochemical sensors offer simple platforms with high sensitivity (greater than colorimetric detection), selectivity, accuracy, a wide linear range, low cost, inexpensive instrumentation, high compatibility with smart devices, and low sample volume requirements. Furthermore, in contrast to colorimetric assays, electrochemical methods offer a unique advantage: they are not affected by the color/turbidity of the sample matrix, which is often the cause of interference.<sup>48–50</sup> Therefore, both types of detection, electrochemical and colorimetric, can complement each other by allowing the conversion of two independent signals, improving the reliability, sensitivity, and portability of future POCT tools for the analysis of relevant analytes.

In previous work by the authors, a PAD was developed to evaluate TSAT in serum samples, based on the colorimetric determination of Tf-bound iron using a smartphone-based color reader.<sup>33</sup> The approach showed high accuracy ( $E_r < 4\%$ ) and a good correlation ( $r = 0.93$ ) with a reference method (urea-PAGE) for the analysis of serum samples from ischemic stroke patients. However, TIBC was measured by adding an excess amount of ferric iron to the serum sample (direct method), implying a multistep approach with intensive analyst intervention.

In this work, a strategy to measure the Tf-bound iron that has already been developed<sup>33</sup> is combined with the electrochemical determination of Tf on a  $\mu$ PAD with colorimetric-electrochemical detection (dual  $\mu$ PAD) using anti-transferrin immunomagnetic beads (anti-Tf-MBs). This dual approach benefits from two independent signal conversions, simplifies the process, improves the sensitivity and selectivity, and stores several reagents on the  $\mu$ PAD (reagent-free device). The design of the  $\mu$ PAD was carried out using low-cost technologies such as tracing with hydrophobic ink on paper, allowing the desired flow of liquids, modification of electrodes through stencil-printing, and impregnation of chemicals for a reagent-free device. Several factors such as reagent volume, electrolyte, carbon ink, voltammetry parameters, among others were optimized to achieve the simultaneous quantification of Tf and Tf-bound iron, and therefore TSAT, with minimal analyst intervention. Finally, this method was validated using a certified reference material (human serum) and successfully compared with a well-established interference-free method (urea-PAGE) toward the analysis of complex samples from ischemic stroke patients.

## Material and methods

### Reagents, materials, and samples

Iron(III) chloride hexahydrate, hydroxylamine hydrochloride, ferrozine (3-(2-pyridyl)-5,6-diphenyl-1,2,4-triazine-*p,p'*-sulfonic acid monosodium salt hydrate), human transferrin (T3309),

human serum, sodium hydroxide, acetic acid glacial, sodium acetate anhydrous, potassium hexacyanoferrate(II) trihydrate, and silver/silver chloride (60/40) paste were purchased from Merck (Darmstadt, Germany). Ortho-phosphoric acid, potassium chloride, and disodium hydrogen phosphate were purchased from Scharlau (Barcelona, Spain). Sodium dihydrogen phosphate and potassium hexacyanoferrate(III) were purchased from PanReac (Barcelona, Spain). Boric acid was acquired from Fluka (Darmstadt, Germany). Carbon paste (BG04) was purchased from SunChemical (New Jersey, USA). Carbon ink (LOCTITE EDAG PF407A) was acquired from Henkel (Düsseldorf, Germany). Disposable screen-printed carbon electrodes (SPCE DRP-110) were purchased from Metrohm (Madrid, Spain). Pierce™ Protein G Magnetic Beads and sodium chloride were acquired from Thermo Fisher Scientific (USA). Human serum (certified reference material, Spintrol H normal 1002121) was purchased from Spinreact (Girona, Spain). Anti-transferrin antibody (ab66952) was purchased from Abcam (Cambridge, UK).

A stock solution of 2 M acetate buffer pH 4.8 was prepared by dissolving appropriate amounts of acetic acid and sodium acetate in Milli-Q water. A stock solution of 0.2 M Britton–Robinson (BR) buffer pH 3.0 was prepared by dissolving appropriate amounts of boric acid 0.04 M, ortho-phosphoric acid 0.04 M, and acetic acid 0.04 M in Milli-Q water adjusting the pH with sodium hydroxide 0.2 M. A stock solution of 0.1 M phosphate buffer saline (PBS) pH 7.4 was prepared by dissolving appropriate amounts of sodium dihydrogen phosphate, disodium hydrogen phosphate, sodium chloride, and potassium chloride in Milli-Q water. The solution of hydroxylamine was prepared by dissolving appropriate amounts in 2 M acetate buffer pH 4.8 to a concentration of 100 mg mL<sup>−1</sup>. The solution of ferrozine was prepared by dissolving appropriate amounts in 2 M acetate buffer pH 4.8 to a concentration of 49 mg mL<sup>−1</sup>. Iron(III) and Tf standard solutions were daily prepared by dissolving appropriate amounts in 0.2 M BR buffer solution of pH 3.0. All reagents and solvents were of analytical grade. All solutions were prepared in Milli-Q water (Merck Millipore, Darmstadt, Germany).

Whatman Chromatography Paper 1 CHR was purchased from Merck (Darmstadt, Germany). Invitrogen™ DynaMag™-2 Magnet was purchased from Thermo Fisher Scientific (USA). The waterproof marker pen Lumocolor® permanent CD/DVD/BD 310 was purchased from Staedtler (Nuremberg, Germany). Tesa 4024 clear packing tape, adhesive vinyl sheets from Tavolozza, and Samtian F40II Lightbox with LED were purchased from Amazon (Spain).

Pseudonymized serum samples of the multicenter, randomized, double-blind, placebo-controlled TANDEM-1 (ref. 29) (thrombolysis and deferoxamine in middle cerebral artery occlusion) study were used to evaluate TSAT by dual  $\mu$ PAD and compared with the urea-PAGE method used by Teresa Gasull's group.<sup>30</sup> The serum samples used were specifically those collected at the Hospital Universitari Germans Trias i Pujol (HUGTP) in untreated patients. All samples were stored at −20 °C before use. TANDEM-1 study was approved by the Spanish



Drug Agency (eudraCT 2007-0006731-31) and by local Ethics Committees, including the HUGTP Ethics Committee, and was registered on <https://clinicaltrials.gov> as NCT00777140.

### Instrumentation

AutoCAD 2018 (Autodesk, student version) was used to design all the components of the  $\mu$ PAD.  $\mu$ PAD design was drawn on a sheet of filter paper (Whatman 1 CHR) using a desktop cutting plotter (Silhouette Cameo 3, Silhouette). The stencils of the Ag/AgCl connections and the reference electrode and of the carbon working and counter electrodes were cut on adhesive vinyl using a desktop cutting plotter (Silhouette Cameo 3, Silhouette). Photos were taken using a Realme X2 mobile and a lightbox (dimensions  $44 \times 44 \times 44$  cm, including 84 brightness LED light beads inside). Subsequent image analysis was performed by ImageJ software. Potentiostat Autolab PGSTAT101 (Metrohm-Autolab, the Netherlands) was used for all the electrochemical measurements. Currents were recorded and displayed on a laptop by using the software Nova 2.1.5. An incubator (Eppendorf ThermoMixer C, Hamburg, Germany) was used for the immunopurification assays.

### Procedures

**Dual  $\mu$ PAD design and fabrication.** Whatman 1 CHR was used as the filter paper because it is hydrophilic, biocompatible, homogeneous, cheap, and reproducible.<sup>51</sup>

Fig. S1 (see the ESI†) shows the schematic procedure of the  $\mu$ PAD fabrication, which consists of three steps:<sup>48</sup>

(i) The dual  $\mu$ PAD patterns were drawn using AutoCAD software (Fig. S1A,† top). This pattern was transferred to a piece of filter paper using a cutter plot, in which the blade was replaced by a waterproof marker pen. Here, the waterproof marker pen ink penetrates the paper to form hydrophobic walls on the filter paper. In addition, it was painted with a thicker waterproof marker pen to mark the part that will delimit the electrochemical cell with its connectors, defining the testing area and confining the solution in the delimited area, thus avoiding its diffusion towards the electrical connections, and affecting the readout (Fig. S1B,† top).

(ii) Next, in the same way as in (i), the three-electrode pattern of Ag/AgCl and carbon was transferred to an adhesive vinyl sheet using a blade as an electrode cutter (Fig. S1A,† middle and bottom, respectively). So these Ag/AgCl and carbon adhesive vinyl patterns were stuck on the piece of filter paper where the  $\mu$ PADs were drawn (Fig. S1B,† middle and bottom, respectively). After, the three-electrode system was manually stencil-printed onto the hydrophilic semicircular electrochemical detection reservoir (Fig. S1C†) using a squeegee and two adhesive vinyl masks (one for Ag/AgCl pattern and the other for carbon pattern). Firstly, the adhesive vinyl mask with the Ag/AgCl pattern was pasted on the filter paper and a layer of Ag/AgCl ink was applied, with the help of a flat squeegee, to create the reference electrode and the electrical connections. The devices were allowed to cure at 90 °C for 30 minutes in an oven (Conterm J.P. Selecta, Barcelona, Spain) and after that time, the

adhesive vinyl was removed with the help of a hot air dryer (Braun Cosmo 1000, Basingstoke, United Kingdom). Secondly, the adhesive vinyl mask with the carbon pattern was pasted on the filter paper and a layer of carbon ink was applied, with the help of a flat squeegee, to create the working and counter electrodes. The devices were allowed to cure at 120 °C for 30 minutes in an oven and after that time, the adhesive vinyl was removed with the help of a hot air dryer. Thermal curing was necessary to make the printed ink stable for the electrochemical measurements. Finally, dual  $\mu$ PADs were individually cut and the backside of the printing surface was covered with clear packing tape (without covering electrical connections) to prevent the solution from leaking out underneath the dual  $\mu$ PAD.

(iii) To produce a reagent-free  $\mu$ PAD, the colorimetric detection reservoir was impregnated with a hydroxylamine solution, as a reducing agent, and a ferrozine solution, as a colorimetric agent (Fig. S1D,† left). Hydroxylamine and ferrozine are commonly used for iron assays as a reducing agent and colorimetric agent, respectively.<sup>52–56</sup> Three depositions of 10  $\mu$ L ( $3 \times 10 \mu$ L) of 100 mg mL<sup>−1</sup> hydroxylamine in 2 M acetate buffer pH 4.8 and 0.5  $\mu$ L of 49 mg mL<sup>−1</sup> ferrozine in 2 M acetate buffer pH 4.8 (the optimal conditions of this chromogenic reagent were chosen based on our previous work<sup>57</sup>) were added to the colorimetric detection reservoir of  $\mu$ PAD, and it was dried completely in an oven at 60 °C for 2 min, after each deposition. The depositions were carried out carefully so as not to impregnate the electrochemical reservoir so that the reagents do not interfere with the electrochemical measurements. Finally, a magnet was pasted on the back of the  $\mu$ PAD at the height of the working electrode (Fig. S1D,† right). Then, the dual  $\mu$ PAD was ready to use.

The dual  $\mu$ PAD consists of a hydrophilic microfluidic channel (5 mm length  $\times$  5 mm width) that will connect an electrochemical semicircular detection reservoir (electrochemical cell of 13 mm diameter) with a colorimetric circular detection reservoir (10 mm diameter). The electrochemical cell consists of three 19 mm  $\times$  1 mm (length  $\times$  width) rectangles separated by 1.5 mm that were used for electrical connections, the reference electrode that was an arc of 3 mm  $\times$  1 mm (length  $\times$  width), the working electrode that was a circle of 4 mm diameter, and the counter electrode that was an arc of 12 mm  $\times$  1 mm (length  $\times$  width). The protective rectangle for connections was 5 mm  $\times$  13 mm (length  $\times$  width). The entire design of the dual  $\mu$ PAD is reported in Fig. S2.†

In a single sheet, 30 devices were drawn and stencil-printed. Then this sheet was cut to individually obtain the corresponding dual  $\mu$ PADs.

**Immunopurification step for Tf isolation and Tf-bound iron release in serum samples.** Anti-Tf-MBs were used for the isolation of Tf (and hence, iron) in human serum samples and they were prepared according to the literature,<sup>58,59</sup> as follows: 50  $\mu$ L of 7.5  $\mu$ g mL<sup>−1</sup> anti-Tf antibody solution prepared in 0.1 M PBS solution pH 7.4 was added to 5  $\mu$ L of immunomagnetic beads (MBs) and incubated for 45 min at 25 °C and 950 rpm. Afterward, the vial containing the anti-Tf-



MBs complex was placed on the magnet holding block for 2 min and then the supernatant was removed. Finally, two washing steps were carried out with 100  $\mu\text{L}$  of 0.1 M PBS solution pH 7.4. The next step allowed us to isolate Tf (and therefore, Tf-bound iron) from the rest of the interferences and potential  $\text{Fe}^{3+}$  species present in the serum matrix, ensuring that we only measured Tf-bound iron: the previously washed vial containing anti-Tf-MBs was resuspended in 90  $\mu\text{L}$  of the human serum sample, which contained Tf, and then it was incubated for 45 min at 25  $^{\circ}\text{C}$  and 950 rpm. Next, in the same way as before, the vial was placed on the magnet holding block for 2 min and then, the supernatant was removed. Two washing steps were carried out with 100  $\mu\text{L}$  of 0.1 M PBS solution of pH 7.4. The final step allowed us to preconcentrate the Tf (and therefore, Tf-bound iron) 3-fold and release the Tf-bound iron into acidic medium, as follows: the Tf-anti-Tf-MBs were resuspended in 30  $\mu\text{L}$  of 0.2 M BR buffer pH 3.0 for 15 min in an incubator at 25  $^{\circ}\text{C}$  and 950 rpm to release the iron from Tf. Finally, these 30  $\mu\text{L}$  samples were transferred to the electrochemical detection reservoir, with Tf-anti-Tf-MBs being retained on the working electrode of the electrochemical cell (since it has a magnet on the back of the  $\mu\text{PAD}$ ) for the electrochemical detection and the rest of the solution (which contains the  $\text{Fe}^{3+}$  ions) flowing through the cellulosic network of filter paper towards the colorimetric detection reservoir where the colorimetric reaction occurs.

**Electrochemical detection of Tf using dual  $\mu\text{PAD}$ .** All electrochemical measurements were carried out by placing a magnet behind the working electrode of the electrochemical cell of the  $\mu\text{PAD}$  to retain Tf-anti-Tf-MBs. 30  $\mu\text{L}$  of the sample (the minimum volume of the electrochemical cell), after the immunopurification step, was transferred to the electrochemical detection reservoir for the measurements. Electrochemical detection to measure Tf was performed using square wave voltammetry (SWV). SWV was carried out in a range potential from +0.3 to +1.4 V, with a step potential of 0.005 V, amplitude of 0.05 V, and frequency of 200 Hz. Control (MBs, anti-Tf, and anti-Tf-MBs) and blank (0.2 M BR buffer pH 3.0) samples were also prepared and analyzed in the same way. All measurements were performed in triplicate using three independent  $\mu\text{PADs}$ .

**Colorimetric detection of Tf-bound iron using dual  $\mu\text{PAD}$ .** The colorimetric assay principle is based on three reactions. Firstly, Tf-bound iron is released from Tf in acidic medium. Next,  $\text{Fe}^{3+}$  ions are reduced to  $\text{Fe}^{2+}$  by a reducing agent. Finally,  $\text{Fe}^{2+}$  ions form a colored complex in the presence of a chromogenic agent.<sup>36,57</sup> The assay was as follows: once 30  $\mu\text{L}$  of the sample was deposited in the electrochemical detection reservoir, Tf-anti-Tf-MBs were retained on the working electrode of the electrochemical cell due to the influence of the magnet attached to the back of the  $\mu\text{PAD}$  and the supernatant of the sample (which contains the released  $\text{Fe}^{3+}$  ions), flowed through the device towards the colorimetric detection reservoir. In this reservoir and in the microfluidic channel, the reduction from  $\text{Fe}^{3+}$  to  $\text{Fe}^{2+}$  happened due to the reducing agent hydroxylamine being previously impregnated

in the paper and, after 10 min at room temperature, the paper turned purple due to the reaction between  $\text{Fe}^{2+}$  and ferrozine (also previously loaded in the paper). The intensity of the purple color obtained in the colorimetric detection reservoir was directly proportional to the concentration of iron in the sample. For both (the  $\text{Fe}^{3+}$  standard solutions used for the calibration curves and the serum samples), a blank (0.2 M BR buffer pH 3) was also prepared and analyzed in the same way as the rest of the samples. The color intensity obtained for the blank was subtracted from the color intensity obtained for each sample. The images of the colorimetric detection reservoirs of the dual  $\mu\text{PADs}$  were taken using a professional photography box with a smartphone (Realme X2) placed on top at 22 cm of dual  $\mu\text{PAD}$ , ensuring the same reservoir-smartphone camera distance. Subsequently, the images were analyzed by ImageJ software in RGB color format and processed as follows: the green channel was selected to measure the intensity of the color because it provides the maximum intensity since the colored product of the reaction of ferrozine with iron is purple (the complementary color). Finally, the image was inverted (pure white and black backgrounds were considered 0- and 255-pixel intensity, respectively), and the colorimetric detection zone of the dual  $\mu\text{PAD}$  was selected individually (circular diameter of 60 pixels) to calculate the mean intensity of the selected area, subtracting the blank value.

**TSAT assay using dual  $\mu\text{PAD}$ .** The  $\mu\text{PAD}$  contains two detection reservoirs: one for the electrochemical detection of Tf and the other for the colorimetric Tf-bound iron measurement. Since TIBC can be calculated by multiplying the Tf concentration (in  $\text{g L}^{-1}$ ) by a conversion factor (1.4 for TIBC in  $\mu\text{g mL}^{-1}$ ) and Tf-bound iron is calculated directly by colorimetry, TSAT is calculated by dividing the concentration of Tf-bound iron by TIBC ( $\mu\text{g mL}^{-1}$ ), as follows:

$$\begin{aligned}\text{TSAT (\%)} &= \frac{[\text{Tf-bound iron}]}{[\text{TIBC}]} \times 100 \\ &= \frac{[\text{Tf-bound iron}]}{[\text{Tf}] \times 1.4} \times 100\end{aligned}\quad (3)$$

## Results and discussion

### Analytical design and development of the dual $\mu\text{PAD}$ for TSAT assessment

As discussed in the introduction section, the assessment of the TSAT biomarker is essential in the clinical field, where both clinical parameters (Tf-bound iron and TIBC) are detected in independent and non-simplified manners. Here we proposed a  $\mu\text{PAD}$  simplifying and integrating the dual/simultaneous determination of both parameters.

Fig. 1 shows the  $\mu\text{PAD}$  designed to integrate this dual determination approach, calculating the ratio between Tf-bound iron (colorimetric) and TIBC through the Tf concentration (electrochemical) measurements (eqn (3)) to obtain the TSAT clinical parameter in a fast and reliable



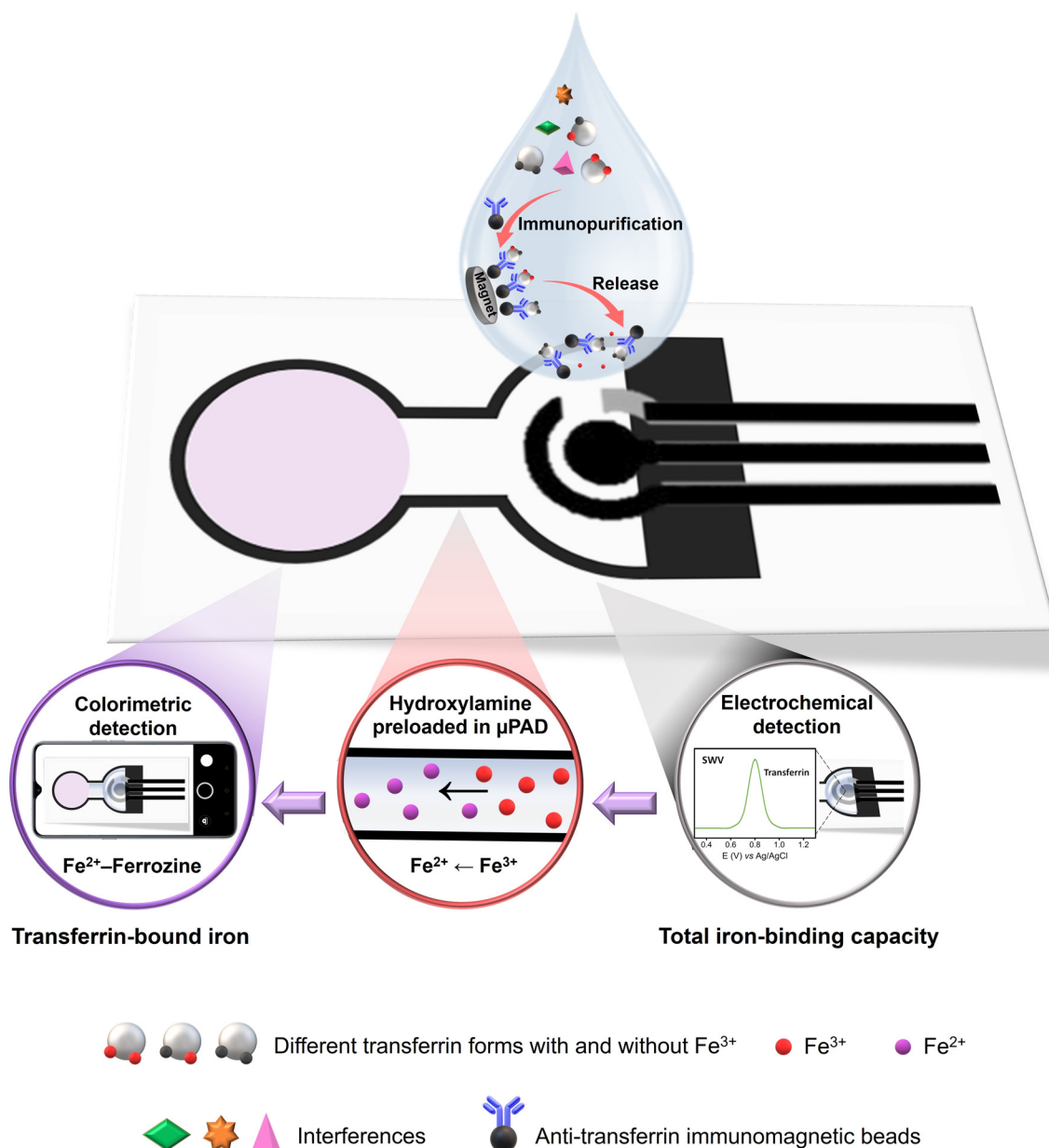


Fig. 1 Dual strategy for the determination of TSAT using anti-Tf-MBs, the electrochemical sensor, and the smartphone-μPAD sensor.

manner. Indeed, this strategy could provide an improvement in the reliability of the analysis benefiting from the independent signal principle and processing. To this end, the sample (with Tf isolated and preconcentrated from the sample using anti-Tf-MBs to ensure that only Tf-bound iron was measured) was intentionally deposited in the electrochemical reservoir to immediately perform the TIBC assessment by exploiting the inherent electroactivity of Tf, allowing the sample to flow through the cellulosic reactor-microfluidic channel (which connects both the detection modes with additionally stored hydroxylamine), where the reduction reaction from  $\text{Fe}^{3+}$  to  $\text{Fe}^{2+}$  in channel occurs and finally the sample reaches the colorimetric detection reservoir (with stored ferrozine), where the formation of the  $\text{Fe}^{2+}$ -ferrozine complex occurs (adapted

from ref. 57) (see Fig. 1). Subsequently, this μPAD was ready to be used and become a useful reagent-free device very suitable for *point-of-care* (POC) applications.

#### Analytical performance of the dual μPAD

To obtain the best analytical performance of the dual μPAD and a reagent-free device, different electrochemical and colorimetric parameters were optimized (see ESI† for full optimization details). Table 1 summarizes all the optimizations performed and the best result obtained in each detection principle optimization.

After optimizing the conditions, the analytical performance of the dual μPAD was evaluated. Linear calibration plots were





**Table 1** Optimization of electrochemical and colorimetric parameters for Tf and Tf-bound iron detection, respectively, using dual  $\mu$ PAD ( $n = 3$ )

Electrochemical parameters		
Parameter	Studied interval	Optimal value
Commercial carbon ink	SunChemical Henkel	SunChemical (Fig. S3A and B†)
Number of Ag/AgCl and carbon ink layers	1 layer of Ag/AgCl + 1 layer of carbon ink 1 layer of Ag/AgCl + 2 layers of carbon ink 2 layers of Ag/AgCl + 1 layer of carbon ink 2 layers of Ag/AgCl + 2 layers of carbon ink	1 layer of Ag/AgCl + 1 layer of carbon ink (Fig. S3C†)
Volume of electrochemical cell	20–50 $\mu$ L	30 $\mu$ L (Fig. S4A†)
Electrochemical technique	SWV DPV	SWV (Fig. S4B†)
Frequency of SWV	50–400 Hz	200 Hz (Fig. S4C†)
Acidic medium	2 M acetate buffer pH 4.8 0.2 M BR buffer pH 3.0	0.2 M BR buffer pH 3.0 (Fig. S5A†)
Colorimetric parameters		
Parameter	Studied interval	Optimal value
Volume of hydroxylamine	1–30 $\mu$ L	$3 \times 10$ $\mu$ L (30 $\mu$ L) (Fig. S6†)

constructed independently for the analysis of Tf and  $\text{Fe}^{3+}$  standard solutions (in 0.2 M BR buffer pH 3.0), by electrochemical and colorimetric detection, respectively (see Fig. 2). Each point on the calibration plots corresponds to the use of three independent dual  $\mu$ PADs.

For electrochemical detection, the calibration curves were built by SWV using the signal generated by the accessible electroactive amino acids present in Tf such as cysteine, tryptophan, and tyrosine<sup>60–62</sup> (at +0.8 V, without any interference of  $\text{Fe}^{3+}$ , see Fig. S5B†) from 0.25  $\text{g L}^{-1}$  to 10  $\text{g L}^{-1}$  (Fig. 2A), obtaining an excellent linear correlation coefficient

( $r = 0.997$ ). The calibration slope was  $1.27 \pm 0.05 \mu\text{A L g}^{-1}$  and the intercept was  $1.1 \pm 0.3 \mu\text{A}$ . The reproducibility of dual  $\mu$ PADs in terms of calibration slopes was very good (RSD = 4%). The limit of detection (LOD) was 0.061  $\text{g L}^{-1}$  (calculated as 3 S/N criteria, using the standard deviation of the point of lowest concentration). In this sense, the LOD was satisfactory for Tf detection in human serum samples, because the normal range for Tf in human blood is between 2 and 3  $\text{g L}^{-1}$ .<sup>63,64</sup>

For colorimetric detection, the color tone gradually varied from colorless to purple with increasing iron concentration, as

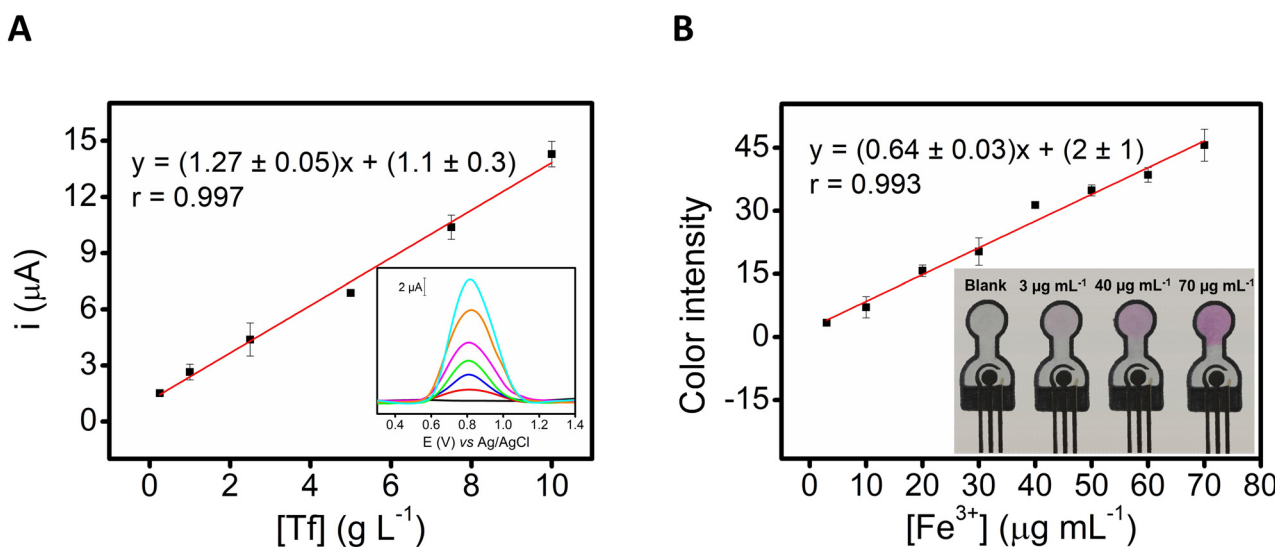


**Fig. 2** (A) Calibration plot of current intensity versus the concentration of Tf. Inset: Voltammograms corresponding to 30  $\mu\text{L}$  of 0.2 M BR buffer pH 3.0 (black line), 0.25  $\text{g L}^{-1}$  Tf (red line), 1  $\text{g L}^{-1}$  Tf (blue line), 2.5  $\text{g L}^{-1}$  Tf (green line), 5  $\text{g L}^{-1}$  Tf (purple line), 7.5  $\text{g L}^{-1}$  (orange line), and 10  $\text{g L}^{-1}$  Tf (cyan line). SWV parameters: start potential +0.3 V, end potential +1.4 V, frequency 200 Hz, amplitude 0.05 V, and step potential 0.005 V (the background signal was linearized) ( $n = 3$ ). (B) Calibration plot of color intensity versus the concentration of  $\text{Fe}^{3+}$ . Inset: Image of dual  $\mu$ PADs used for calibration. Experimental conditions: 30  $\mu\text{L}$  of  $\text{Fe}^{3+}$  standard solution from 3  $\mu\text{g mL}^{-1}$  to 70  $\mu\text{g mL}^{-1}$  in 0.2 M BR buffer pH 3.0. 2 min reaction time ( $n = 3$ ).





shown in the inset of Fig. 2B. The calibration curve for iron was linear in the range of 3–70  $\mu\text{g mL}^{-1}$ , showing an excellent correlation coefficient ( $r = 0.993$ ). The calibration slope was  $0.64 \pm 0.03 \text{ px mL } \mu\text{g}^{-1}$  and the intercept was  $2 \pm 1 \text{ px}$ . The reproducibility of dual  $\mu\text{PADs}$  in terms of calibration slopes was also good ( $\text{RSD} = 5\%$ ). However, LOD was  $2 \mu\text{g mL}^{-1}$  (calculated as 3 S/N criteria, using the standard deviation of the point of lowest concentration), which is slightly higher than the levels of iron present in human serum (normal range from 0.7 to  $1.7 \mu\text{g mL}^{-1}$ ).<sup>65</sup> But this was not a problem when the serum samples were analyzed because the Tf immunopurification step not only allowed the removal of the potential interferences but also preconcentrated the sample 3-fold (90  $\mu\text{L}$  serum is concentrated in a 30  $\mu\text{L}$  solution), thus allowing its quantification and improving the accuracy of TSAT assessment (see section Immunopurification step for Tf isolation and Tf-bound iron release in serum samples). So, the LOD of the overall method was reduced from 2 to  $0.67 \mu\text{g mL}^{-1}$ .

When analyzing serum samples, an immunopurification process is necessary to isolate Tf from the rest of the components of the sample. However, antibodies are glycoproteins and can be electroactive, so it is necessary to perform electrochemical measurements by SWV to several controls (MBs in 0.2 M BR buffer pH 3.0,  $7.5 \mu\text{g mL}^{-1}$  anti-Tf antibody in 0.2 M BR buffer pH 3.0, and anti-Tf-MBs in 0.2 M BR buffer pH 3.0) and a blank (0.2 M BR buffer pH 3.0). As can be seen in Fig. S7†, the signal obtained for the anti-Tf antibody (Fig. S7†, purple line) is negligible compared to the peak at +0.8 V of Tf in the commercial serum sample after the immunopurification step without a preconcentration step (Fig. S7†, green line). In addition, the antibody concentration used was in excess but after incubation with the MBs, the excess was eliminated by washing. As can be seen in the controls using MBs and anti-Tf-MBs (Fig. S7†, red line and blue line, respectively) there was no anodic peak for the controls analyzed. Therefore, it is possible to use these anti-Tf and MBs in the immunopurification process. It was necessary to place a magnet on the back of the dual  $\mu\text{PAD}$  on the working electrode since MBs are brown and must be retained on the working electrode so that they do not mask the colorimetric signal obtained in the  $\text{Fe}^{3+}$  assay.

Then the dual  $\mu\text{PAD}$ -based approach was validated for both parameters (Tf-bound iron and Tf) by the analysis of a certified reference material (human serum) using the external calibration method ( $n = 3$ ). The results are collected in Table 2.

Based on these results, our approach showed excellent accuracy and precision. Furthermore, both parameters were

measured on the same dual  $\mu\text{PAD}$ , demonstrating its multiplexing capacity and highlighting its robustness combined with the low-cost manufacturing process of the dual  $\mu\text{PADs}$ .

The stability of the reagent-free  $\mu\text{PAD}$  was also evaluated. Several dual  $\mu\text{PADs}$  were prepared and stored in plastic zipper bags at room temperature in the dark, to limit the oxidation of silver and degradation of the preloaded reagents on the dual  $\mu\text{PAD}$  due to light exposure. The stability of the electrochemical detector was evaluated over time by measuring the anodic peak intensity of a 5 mM ferro/ferri system solution by cyclic voltammetry (with three different dual  $\mu\text{PADs}$ ). Impressively, after one year, there were no significant differences in the electrochemical signal concerning the anodic peak intensity obtained on the first day ( $t$ -test,  $\alpha = 0.05$ , two sides), demonstrating its long stability over time (see Fig. S8†). However, the colorimetric assay was a limiting factor since it was stable for 40 days,<sup>33</sup> being also a valuable one. This limitation is not a problem *per se*, for commercial purposes, because both reagents can be added to the  $\mu\text{PAD}$  when performing the colorimetric assay.

#### Assessment of TSAT in serum samples from ischemic stroke patients by using the dual $\mu\text{PAD}$

Once the good analytical performance of the dual  $\mu\text{PAD}$  for the simultaneous determination of Tf and  $\text{Fe}^{3+}$  was demonstrated, under optimal conditions, the reagent-free dual  $\mu\text{PAD}$  was evaluated for TSAT determination in 9 pseudonymized serum samples from ischemic stroke patients of the TANDEM-1. The results obtained for the TSAT values are shown in Fig. 3A where they were also compared with those obtained by the urea-PAGE method<sup>30</sup> (see also Table S1†). Impressively, both methods, exhibited a good correlation coefficient ( $r = 0.96$ ) and no significant differences were found since the values obtained for the slope ( $1.0 \pm 0.1$ ) and the intercept ( $1 \pm 4$ ), included 1 and 0, respectively ( $p < 0.05$ ); consequently, revealing an excellent accuracy since the urea-PAGE method is a free-interference method (see a visual example in Fig. 3B).

In addition, these results were compared with those obtained by our previously reported method based on a colorimetric PAD for the detection of TSAT<sup>33</sup> (Fig. 3C), showing great similarities in the analysis of the same samples. Interestingly, the values provided by the dual  $\mu\text{PAD}$  are closer to the reference values (urea-PAGE) than those provided by our previous colorimetric  $\mu\text{PAD}$  for most of the cases. This means that the dual approach improved the method accuracy thanks to the electrochemical detection, which offers higher accuracy than colorimetric detection for the measurement of TIBC. These

**Table 2** Analysis of certified reference material by the dual  $\mu\text{PAD}$  ( $n = 3$ )

Parameter	Certified value	Dual $\mu\text{PAD}$ value		
		$\bar{x} \pm s$	RSD (%)	$E_r$ (%)
Serum iron	$1.13 \mu\text{g mL}^{-1}$	$1.08 \pm 0.01 \mu\text{g mL}^{-1}$	1	4
Tf	$1.84 \text{ g L}^{-1}$	$1.75 \pm 0.04 \text{ g L}^{-1}$	2	5



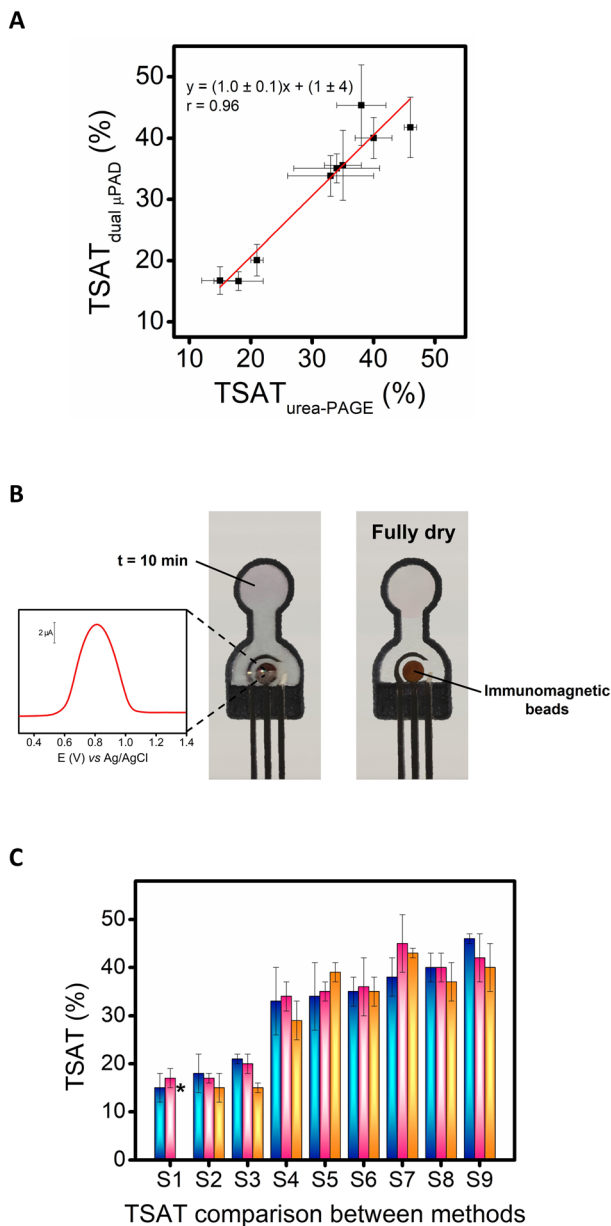


**Fig. 3** (A) Correlation between TSAT values obtained by dual  $\mu$ PAD and by urea-PAGE<sup>30</sup> ( $n = 3$ ). (B) Image of a dual  $\mu$ PAD used for sample S5 for the TSAT assessment using its two parameters: SWV for Tf (electrochemical detection) and  $\text{Fe}^{2+}$ -ferrozine complex formation at 10 min (colorimetric detection) (left), and image of the same dual  $\mu$ PAD when it dries completely and the MBs are observed fully retained on the working electrode (brown circle) (right). Experimental condition: see section Procedures (the background signal was linearized) ( $n = 3$ ). (C) Comparison in TSAT analysis between the urea-PAGE method<sup>30</sup> (blue bar), our approach based on a dual  $\mu$ PAD (pink bar), and the previously reported method based on a colorimetric PAD.<sup>33</sup> \* Sample S1 was not available in the colorimetric PAD.<sup>33</sup>

results demonstrated the suitability of the developed dual  $\mu$ PAD as a reliable microfluidic sensor for the assessment of TSAT using an easy procedure and a cost-effective device. Our approach turned out to be highly competitive compared to current methods since they use expensive benchtop equipment

and are located in clinical laboratories or medical centers,<sup>29,36</sup> and the dual  $\mu$ PAD shown here is cheap, portable, single-use (avoiding cross-contamination), easy-to-use, sensitive, specific, reagent-free, and deliverable to end-users, as well as the fact that it requires a very low clinical sample volume (90  $\mu\text{L}$ ). All these features make our dual detection device a potential candidate for a future POCT for ischemic stroke prognosis. On the other hand, the urea-PAGE method has the advantage of separating and detecting the different forms of Tf-bound iron (apo-Tf, monoferric-Tf, and diferric-Tf) but it is very slow (more than 18 h). Our approach takes less than 90 min and has the advantage of being independent of the color of the sample, thanks to the use of anti-Tf-MBs, so serum, blood, or hemolyzed samples may be analyzed.

In recent years, other authors have explored the extraordinary advantages of dual PADs combining colorimetry and electrochemical detection for detecting analytes of clinical relevance. The general characteristics of these devices are summarized in Table S2.†

In most cases, dual sensing devices integrating colorimetric and electrochemical detection have benefited from the excellent sensitivity and selectivity of electrochemical detection along with the simplicity of colorimetric techniques, despite their limited sensitivity. This approach has been used to develop devices with a hybrid sensing mode for the same analyte with the specific objective of expanding the working range in the practical detection in clinical applications.<sup>66–69</sup> However, more interesting approaches involve analyzing different analytes simultaneously within a single integrated device to obtain a more comprehensive response, providing more information for clinical evaluation. For example, a colorimetric and electrochemical dual  $\mu$ PAD for the simultaneous detection of several biomarkers of periodontitis disease in saliva,<sup>70</sup> or the one developed in this work for determining the TSAT (%) parameter through the selective and sensitive electrochemical detection of Tf (TIBC) and the colorimetric detection of  $\text{Fe}^{3+}$  (Tf-bound iron) in real human serum samples from patients who have suffered an ischemic stroke.

## Conclusions

A novel dual  $\mu$ PAD was successfully developed for the assessment of TSAT in serum samples by the ratio between Tf-bound iron, which was assayed by a colorimetric approach, and TIBC, which was evaluated by an electrochemical approach. The use of electrochemical detection provided higher simplicity and accuracy to the approach since TIBC was directly measured by exploiting the inherent Tf electroactivity. Moreover, all reagents needed for the colorimetric approach were stored on the  $\mu$ PAD, yielding a reagent-free device, which is ready to be used. These dual  $\mu$ PADs were successfully applied to the analysis of serum samples from ischemic stroke patients, showing excellent accuracy in comparison to a free-interference method (urea-PAGE) and revealing key advantages such as low sample volumes and short analysis times required. Therefore, the developed dual  $\mu$ PAD may be a promising POCT device to assist



physicians in the fast prognosis of ischemic stroke, where the decision-making time is crucial. In this sense, future research would be to perform the immunopurification process on the surface of the working electrode, creating a ready to use POCT device and simplifying the number of steps for analysis. Moreover, the concept of colorimetric and electrochemical  $\mu$ PAD could pave the way to new applications not only in clinical diagnostics and POC technologies but towards others belonging to the *point-of-need* in environmental and food as well as environmental forensic fields, because the possibility of performing two different detection modes provides higher flexibility and multiplexing capabilities since analysts can choose the best detection mode for each kind of target analyte.

## Data availability

The data supporting this article have been included as part of the ESI†

## Author contributions

S. D.: conceptualization, investigation, methodology, formal analysis, visualization, validation, writing–original draft, writing–review & editing. M. P.: conceptualization, investigation, methodology, formal analysis, visualization, validation, writing–original draft, writing–review & editing. A. G. C.: conceptualization, investigation, formal analysis, supervision, writing–original draft, writing–review & editing. T. G.: conceptualization, resources, writing–review & editing. A. E.: conceptualization, investigation, project administration, funding acquisition, resources, formal analysis, supervision, writing–review & editing.

## Conflicts of interest

There are no conflicts to declare.

## Acknowledgements

This work has been financially supported by the TRANSNANOAVANSENS program from the Community of Madrid (P2018/NMT-4349) (A. E.), by the grant PID2020-118154GB-I00 funded by MCIN/AEI/10.13039/501100011033 (A. E.), by the NEURO-CHIP-CM program from the Community of Madrid (Y2020/NMT6312) (A. E.), by the RICORS RD21/0006/0024 (NextGeneration EU funding) and 2021SGR00925 (Agencia de gestió d'Ajuts Universitaris i de Recerca de Catalunya) (T. G.), and by the Spanish Ministry of Economy and Competitiveness (CTQ2017-86441-C2-1-R, FPI fellowship (S. D.)).

## References

- WHO EMRO|Stroke, Cerebrovascular accident|Health topics, <https://www.emro.who.int/health-topics/stroke-cerebrovascular-accident/index.html>.
- S. K. Feske, *Am. J. Med.*, 2021, **134**, 1457–1464.
- E. C. Jauch, J. L. Saver, H. P. Adams, A. Bruno, J. J. B. Connors, B. M. Demaerschalk, P. Khatri, P. W. McMullan, A. I. Qureshi, K. Rosenfield, P. A. Scott, D. R. Summers, D. Z. Wang, M. Wintermark and H. Yonas, *Stroke*, 2013, **44**, 870–947.
- P. Vilela, *Eur. J. Radiol.*, 2017, **96**, 133–144.
- G. McClelland, H. Rodgers, D. Flynn and C. I. Price, *Eur. J. Emerg. Med.*, 2019, **26**, 2–8.
- S. J. Allder, A. R. Moody, A. L. Martel, P. S. Morgan, G. S. Delay, J. R. Gladman, P. Fentem and G. G. Lennox, *Lancet*, 1999, **354**, 1523.
- M. Pohl, D. Hesseberger, K. Kapus, J. Meszaros, A. Feher, I. Varadi, G. Pusch, E. Fejes, A. Tibold and G. Feher, *J. Clin. Neurosci.*, 2021, **93**, 174–182.
- S. Sotgiu, B. Zanda, B. Marchetti, M. L. Fois, G. Arru, G. M. Pes, F. S. Salaris, A. Arru, A. Pirisi and G. Rosati, *Eur. J. Neurol.*, 2006, **13**, 505–513.
- J. R. Lynch, R. Blessing, W. D. White, H. P. Grocott, M. F. Newman and D. T. Laskowitz, *Stroke*, 2004, **35**, 57–63.
- M. A. Reynolds, H. J. Kirchick, J. R. Dahlen, J. M. Anderberg, P. H. McPherson, K. K. Nakamura, D. T. Laskowitz, G. E. Valkirs and K. F. Buechler, *Clin. Chem.*, 2003, **49**, 1733–1739.
- G. C. Jickling and F. R. Sharp, *Neurotherapeutics*, 2011, **8**, 349–360.
- Q. Tan, Y. Fang and Q. Gu, *Front. Pharmacol.*, 2021, **12**, 1–15.
- L. Magtanong and S. J. Dixon, *Dev. Neurosci.*, 2019, **40**, 382–395.
- Z. Geng, Z. Guo, R. Guo, R. Ye, W. Zhu and B. Yan, *Brain Res. Bull.*, 2021, **172**, 212–219.
- D. Gill, G. Monori, I. Tzoulaki and A. Dehghan, *Stroke*, 2018, **49**, 2815–2821.
- Q. He, W. Wang, D. Xu, Y. Xiong, C. You, C. Tao and L. Ma, *Stroke*, 2024, **55**, 423–431.
- C. Bolm, *Nat. Chem.*, 2009, **1**, 420.
- A. N. Luck and A. B. Mason, *Curr. Top. Membr.*, 2012, **69**, 3–35.
- C. P. Anderson, M. Shen, R. S. Eisenstein and E. A. Leibold, *Biochim. Biophys. Acta, Mol. Cell Res.*, 2012, **1823**, 1468–1483.
- D. M. Frazer and G. J. Anderson, *BioFactors*, 2014, **40**, 206–214.
- T. Kamińska-Gibas, J. Szczygiel, P. Jurecka and I. Irnazarow, *Fish Shellfish Immunol.*, 2020, **102**, 511–518.
- M. E. Elsayed, M. U. Sharif and A. G. Stack, *Adv. Clin. Chem.*, 2016, **75**, 71–97.
- H. Li and Z. M. Qian, *Med. Res. Rev.*, 2002, **22**, 225–250.
- J. O. Jeppsson, Structural studies on human transferrin, *Dissertation*, Umeå universitet, 1967.
- N. C. Giri, Role of Transferrin in Iron Metabolism, *Iron Metabolism - A Double-Edged Sword*, 2022.
- J. Parkkinen, L. von Bonsdorff, F. Ebeling and L. Sahlstedt, *Vox Sang.*, 2002, **83**(Suppl 1), 321–326.
- K. Gkouvatsos, G. Papanikolaou and K. Pantopoulos, *Biochim. Biophys. Acta, Gen. Subj.*, 2012, **1820**, 188–202.
- P. Cacoub, C. Vandewalle and K. Peoc'h, *Crit. Rev. Clin. Lab. Sci.*, 2019, **56**, 526–532.
- M. Millán, N. Degregorio-Rocasolano, N. P. de la Ossa, S. Reverté, J. Costa, P. Giner, Y. Silva, T. Sobrino, M. Rodríguez-Yáñez, F. Nombela, F. Campos, J. Serena, J. Vivancos, O. Martí-Sistac, J. Cortés, A. Dávalos and T. Gasull, *Antioxidants*, 2021, **10**, 1270.



- 30 N. DeGregorio-Rocasolano, O. Martí-Sistac, J. Ponce, M. Castelló-Ruiz, M. Millán, V. Guirao, I. García-Yébenes, J. B. Salom, P. Ramos-Cabrer, E. Alborch, I. Lizasoain, J. Castillo, A. Dávalos and T. Gasull, *Redox Biol.*, 2018, **15**, 143–158.
- 31 M. Castellanos, N. Puig, T. Carbonell, J. Castillo, J. M. Martinez, R. Rama and A. Dávalos, *Brain Res.*, 2002, **952**, 1–6.
- 32 I. García-Yébenes, M. Sobrado, A. Moraga, J. G. Zarruk, V. G. Romera, J. M. Pradillo, N. Perez De La Ossa, M. A. Moro, A. Dávalos and I. Lizasoain, *Neurochem. Int.*, 2012, **61**, 1364–1369.
- 33 S. Dorte, N. DeGregorio-Rocasolano, M. Millán, T. Gasull, A. G. Crevillen and A. Escarpa, *Anal. Chem.*, 2023, **95**, 12391–12397.
- 34 S. H. Mehta, R. C. Webb, A. Ergul, A. Tawak and A. M. Dorrance, *Am. J. Physiol.*, 2004, **286**, 283–288.
- 35 H. Yamanishi, S. Kimura, S. Iyama, Y. Yamaguchi and T. Yanagihara, *Clin. Chem.*, 1997, **43**, 2413–2417.
- 36 K. Strzelak, N. Rybkowska, A. Wiśniewska and R. Koncki, *Anal. Chim. Acta*, 2017, **995**, 43–51.
- 37 H. Yamanishi, S. Iyama, Y. Yamaguchi, Y. Kanakura and Y. Iwatani, *Clin. Chem.*, 2003, **49**, 175–178.
- 38 T. Eleftheriadis, V. Liakopoulos, G. Antoniadis and I. Stefanidis, *Renal Failure*, 2010, **32**, 1022–1023.
- 39 C. Frank, O. Rienitz, R. Jähring, D. Schiel and S. Zakel, *Metallomics*, 2012, **4**, 1239–1244.
- 40 N. Kitsati, D. Liakos, E. Ermeidi, M. D. Mantzaris, S. Vasakos, E. Kyrtzopoulou, P. Eliadis, E. Andrikos, E. Kokkolou, G. Sferopoulos, A. Mamalaki, K. Siamopoulos and D. Galaris, *Haematologica*, 2015, **100**, 80–83.
- 41 R. Agarwal, *Kidney Int.*, 2004, **66**, 1139–1144.
- 42 P. B. Lippa, C. Müller, A. Schlichtiger and H. Schlebusch, *TrAC, Trends Anal. Chem.*, 2011, **30**, 887–898.
- 43 W. Zheng, K. Wang, H. Xu, C. Zheng, B. Cao, Q. Qin, Q. Jin and D. Cui, *Anal. Bioanal. Chem.*, 2021, **413**, 2429–2445.
- 44 W. Alahmad, A. Sahragard and P. Varanusupakul, *Biosens. Bioelectron.*, 2021, **194**, 113574.
- 45 T. Ozer, C. McMahon and C. S. Henry, *Annu. Rev. Anal. Chem.*, 2020, **13**, 85–109.
- 46 G. Chen, C. Fang, H. H. Chai, Y. Zhou, W. Yun Li and L. Yu, *Sens. Actuators, B*, 2019, **281**, 253–261.
- 47 G. G. Morbioli, T. Mazzu-Nascimento, A. M. Stockton and E. Carrilho, *Anal. Chim. Acta*, 2017, **970**, 1–22.
- 48 S. Dorte, A. G. Crevillen, A. Escarpa and S. Cinti, *Sens. Actuators, B*, 2024, **398**, 134704.
- 49 Y. Xu, H. Ning, S. Yu, S. Liu, Y. Zhang, C. Niu, Y. Zhang, S. S. Low and J. Liu, *Micromachines*, 2023, **14**, 142.
- 50 K. Mahato and J. Wang, *Sens. Actuators, B*, 2021, **344**, 130178.
- 51 E. Carrilho, A. W. Martinez and G. M. Whitesides, *Anal. Chem.*, 2009, **81**, 7091–7095.
- 52 Z. Miao, X. Gu, S. Lu, M. L. Brusseau, N. Yan, Z. Qiu and Q. Sui, *J. Hazard. Mater.*, 2015, **300**, 530–537.
- 53 G. Bengtsson, S. Fronæus and L. Bengtsson-Kloo, *J. Chem. Soc., Dalton Trans.*, 2002, 2548–2552.
- 54 G. L. Smith, A. A. Reutovich, A. K. Srivastava, R. E. Reichard, C. H. Welsh, A. Melman and F. Bou-Abdallah, *J. Inorg. Biochem.*, 2021, **220**, 111460.
- 55 L. L. Stookey, *Anal. Chem.*, 1970, **42**, 779–781.
- 56 Z. Yang, Y. Yan, A. Yu, B. Pan and J. J. Pignatello, *Chem. Eng. J.*, 2020, **391**, 123592.
- 57 S. Dorte, A. G. Crevillen and A. Escarpa, *Talanta*, 2023, **253**, 123914.
- 58 T. Sierra, C. S. Henry, A. G. Crevillén and A. Escarpa, *Analysis Sensing*, 2022, **2**, 2–8.
- 59 T. Sierra, A. G. Crevillen and A. Escarpa, *Biosens. Bioelectron.*, 2021, **179**, 113098.
- 60 A. H. B. Dourado, F. C. Pastrián and S. I. C. De Torresi, *An. Acad. Bras. Cienc.*, 2018, **90**, 607–630.
- 61 E. V. Suprun, E. V. Karpova, S. P. Radko and A. A. Karyakin, *Electrochim. Acta*, 2020, **331**, 135289.
- 62 K. Moulæe and G. Neri, *Biosensors*, 2021, **11**, 1–54.
- 63 H. Kawabata, *Free Radical Biol. Med.*, 2019, **133**, 46–54.
- 64 P. T. Gomme and K. B. McCann, *Drug Discovery Today*, 2005, **10**, 267–273.
- 65 W. Breuer, C. Hershko and Z. I. Cabantchik, *Transfus. Sci.*, 2000, **23**, 185–192.
- 66 K. Pungjunun, A. Yakoh, S. Chaiyo, N. Praphairaksit, W. Siangproh, K. Kalcher and O. Chailapakul, *Microchim. Acta*, 2021, **188**, 1–11.
- 67 H. Wang, C. Zhou, X. Sun, Y. Jian, Q. Kong, K. Cui, S. Ge and J. Yu, *Biosens. Bioelectron.*, 2018, **117**, 651–658.
- 68 W. Xue, P. Jia, Y. Wu, P. Wang, J. Shi, Y. Chan and M. Liu, *Adv. Agrochem*, 2023, **2**, 269–275.
- 69 J. Xu, J. Shen, B. Zhang, Y. Zhang, X. Lv and G. Zhu, *Electrochim. Acta*, 2024, **481**, 143952.
- 70 L. R. Sousa, H. A. Silva-Neto, L. F. Castro, K. A. Oliveira, F. Figueredo, E. Cortón and W. K. T. Coltro, *Anal. Bioanal. Chem.*, 2023, **415**, 4391–4400.

